

Toward an actual account for the angular dependence of the Brueckner-Bethe-Goldstone propagator in nuclear matter

H. F. Arellano^{1,2,*} and J.-P. Delaroche^{2,†}¹*Department of Physics - FCFM, University of Chile, Av. Blanco Encalada 2008, Santiago, Chile*²*CEA/DAM/DIF, F-91297 Arpajon, France*

(Received 18 February 2011; published 11 April 2011)

Angular correlations arising from particle-particle (pp) propagation in symmetric nuclear matter are investigated. Their account follows a detailed treatment of the angular dependence of the energy denominator of the propagator in the Brueckner-Bethe-Goldstone (BBG) equation, in conjunction with the Pauli exclusion principle for intermediate states. As a result, taking a monopole approximation for the propagator, a correlation form factor emerges from the Cauchy principal-value integral of the pp propagator, while the imaginary part becomes structurally different from those in Lippmann-Schwinger-type equations. These features are investigated within the continuous choice of the single-particle potential considering the Argonne v_{18} and Paris two-nucleon potentials. We find that the behavior of the mass operator is affected, deepening slightly the saturation point of symmetric nuclear matter relative to those based on angle-averaged energy denominators. Implications of these angular correlations were also investigated in the context of proton-nucleus scattering, showing clear effects on scattering observables below 100 MeV.

DOI: [10.1103/PhysRevC.83.044306](https://doi.org/10.1103/PhysRevC.83.044306)

PACS number(s): 21.65.Mn, 21.10.Dr, 24.10.Cn, 21.30.fe

I. INTRODUCTION

The ability to provide accurate predictions of nuclear many-body phenomena, on the basis of meson-exchange models for the nucleon-nucleon (NN) interaction, remains as one of the most challenging goals in nuclear theory. In the Brueckner-Bethe-Goldstone (BBG) theory of nuclear matter, the mass operator has played a pivotal role in microscopic descriptions of various quantities of physical interest [1,2]. At negative energies it has been a basis for extensive studies of saturation properties of symmetric nuclear matter, one of the most elusive puzzles in nuclear physics [3–6]. At positive energies it has been crucial for the development of density-dependent effective interactions, extensively used in microscopic optical potentials for nucleon-nucleus scattering [7,8]. Here, however, the mass operator still lacks adequate consistency to describe the data below 100 MeV without ad hoc rescaling. Another issue which has captured increasing interest in the past decade is the behavior of nuclear matter under extreme isospin asymmetric conditions, such as in the case of neutron stars [9].

An aspect of central importance in the BBG equation for the reaction matrix is the treatment of pp propagation while enforcing the Pauli exclusion principle on intermediate states. The pp propagator is usually represented as the ratio of two commuting operators, $Q/e^{(+)}$, with Q the Pauli blocking operator and $e^{(+)}$ the difference, on the upper edge of the real axis, between a starting energy and intermediate-state single-particle (sp) energies. Major attention has been given to the nonsphericity of the integration domain due to the Pauli operator, while complications arising from the angular depen-

dence of the energy denominator were systematically handled resorting to angular averages or effective-mass approximations [10–14]. Implicit in these approximations is the assumption that the kinematics of intermediate states, as restricted by the Pauli exclusion principle, is uncorrelated from the propagation of the interacting particles under the sp fields. In traditional approaches [1], angular averages of the ratio of the two operators are approximated by the ratio of their averages. However, the stringent self-consistency requirements to the solution of the BBG equation—particularly within the continuous choice [1]—call for a closer scrutiny in the handling of the actual ratio $Q/e^{(+)}$. This was earlier noted by Sartor [15], reporting solutions to the BBG equation with a treatment of the pp propagator in its full form, including angular momentum couplings among different NN states. It was concluded that the explicit treatment of the angular dependence of the energy denominator renders marginal corrections to its angle-averaged form. However, as we shall explain later, the numerical strategies utilized in the referred work become unsuited to resolve concealed features in the angular behavior of the pp propagator. As a matter of fact, unforeseen structures emerge in the propagator when the angular dependence of the *ratio* is retained within a controlled representation, featuring sharp and narrow structures in momentum space that require specific techniques to keep them under control.

This paper is organized as follows: In Sec. II we outline the theoretical framework, describe traditional approaches for the treatment of the angular dependence of the energy denominator, and introduce a way to treat this dependence exactly. Here we also describe numerical strategies to treat accurately sharp structures appearing in the pp propagator. In Sec. III we present the main results from this work, addressing the effect of angular correlations on symmetric nuclear matter properties and on proton-nucleus elastic scattering. In Sec. IV we summarize this work and draw the main conclusions.

* arellano@dfi.uchile.cl

† jean-paul.delaroche@cea.fr

II. THEORETICAL FRAMEWORK

In the BBG theory for symmetric nuclear matter (NM) the g matrix depends on the density of the medium, characterized by the Fermi momentum k_F , and a starting energy ω . If v denotes the bare interaction between two nucleons in an infinite medium, with \hat{h}_1 and \hat{h}_2 their respective quasiparticle energies, then $g(\omega)$ satisfies

$$g(\omega) = v + v \frac{Q}{\omega - \hat{h}_1 - \hat{h}_2 + i\eta} g(\omega). \quad (1)$$

The solution to this equation enables the evaluation of the mass operator

$$M(k; E) = \sum_{|\mathbf{p}| \leq k_F} \langle \frac{1}{2}(\mathbf{k} - \mathbf{p}) | g_{\mathbf{K}}(E + \epsilon_p) | \frac{1}{2}(\mathbf{k} - \mathbf{p}) \rangle, \quad (2)$$

where $\epsilon_p = p^2/2m + U(p)$, the sp energy of nucleons of mass m in terms of an auxiliary field U , and $\mathbf{K} = \mathbf{k} + \mathbf{p}$, the total momentum of any interacting pair. Self-consistency requires that

$$U(k) = \text{Re } M(k; \epsilon_k),$$

which is achieved iteratively. In the continuous choice [1], this condition is imposed to all momenta k .

In momentum representation the BBG equation takes the explicit form

$$\begin{aligned} \langle \kappa' | g_{\mathbf{K}}(\omega) | \kappa \rangle &= \langle \kappa' | v | \kappa \rangle + \int d\mathbf{q} \langle \kappa' | v | \mathbf{q} \rangle \\ &\times \frac{\Theta(k_+ - k_F) \Theta(k_- - k_F)}{\omega + i\eta - \frac{k_+^2}{2m} - \frac{k_-^2}{2m} - \Sigma} \langle \mathbf{q} | g_{\mathbf{K}}(\omega) | \kappa \rangle, \quad (3) \end{aligned}$$

where

$$\Sigma(K, q, x) \equiv U(k_+) + U(k_-), \quad (4)$$

with

$$k_{\pm}^2 = \frac{K^2}{4} + q^2 \pm qKx.$$

Here $x = \hat{\mathbf{K}} \cdot \hat{\mathbf{q}}$, corresponding to the cosine of the angle between \mathbf{K} and \mathbf{q} . The step functions Θ forbid particle propagation below the Fermi surface, as required by the Pauli exclusion principle. Here the Pauli blocking operator takes the representation $Q(\mathbf{K}, \mathbf{q}) = \Theta(k_+ - k_F) \Theta(k_- - k_F)$. The geometry of such exclusion is illustrated in Fig. 1, where we show the restrictions posed on x when $K/2$ lays inside ($K \leq 2k_F$) and outside ($K > 2k_F$) the Fermi sphere. Only those configurations where the arrowheads of the incoming (\mathbf{q}) and outgoing ($-\mathbf{q}$) relative momenta lay outside the sphere are included in the integration domain of \mathbf{q} , a condition met when $|x| \leq \cos \theta_F \equiv \Delta$.

At this point it is useful to denote the energy denominator in Eq. (3) as $e^{(+)} \equiv e + i\eta$, so that the propagator becomes expressed as $Q/e^{(+)}$. Traditionally, its angular dependence together with its coupling to v and g , has been simplified by treating the numerator Q separately from the denominator $e^{(+)}$. A common practice is that of approximating the inverse of the energy denominator $\langle 1/e^{(+)} \rangle$ by the inverse of its average, $1/\langle e^{(+)} \rangle$. If the angular dependence of the Pauli

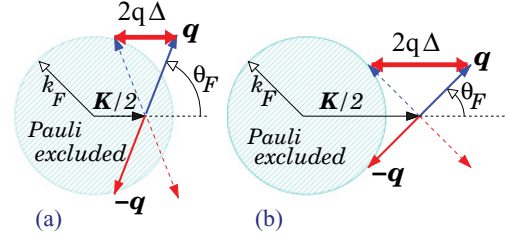


FIG. 1. (Color online) Pauli-principle restrictions on the angular variation of \mathbf{q} for (a) $K < 2k_F$ and (b) $K > 2k_F$. Here $\Delta = \cos \theta_F$.

blocking operator is retained, then the propagator takes the form $Q/\langle e^{(+)} \rangle$, with the nonspherical geometry of the Pauli operator treated in its full form [10–14]. This scheme is sometimes referred to as *exact treatment of the Pauli blocking*, although it does not treat the propagator in its full form since it relies on angular averages of the energy denominator [10,11] or effective-mass approximations for the sp spectrum [13,14]. Current standards go one step further by taking the angular average of the Pauli operator [16], where $Q \rightarrow \langle Q \rangle$, with

$$\langle Q \rangle = \frac{1}{4\pi} \int Q(\mathbf{K}, \mathbf{q}) d\Omega_q = \Delta,$$

and $\Delta = \min\{1, \max[0, (K^2/4 + q^2 - k_F^2)/qK]\}$. Here we use $d\Omega_q = dx d\phi$, with ϕ the azimuth angle in the plane perpendicular to \mathbf{K} . With these approximations $Q/e^{(+)} \rightarrow \langle Q \rangle/e^{(+)}$, and $\langle Q \rangle/e^{(+)} \approx \Delta/\langle e^{(+)} \rangle$, the *ratio of averages* (RAv), named hereafter RAv approximation. These two approximations become best justified when Σ is independent of x , a condition met only if $U(p)$ is quadratic in p . Such is the case of the effective-mass approximation, where it is assumed that the sp spectrum follows a quadratic behavior, $\epsilon_p = p^2/2M^* + U_o$, with M^* an effective mass and U_o a field constant, both quantities calculated self-consistently [1]. The reliability of this approximation has been studied in Ref. [17], where it was shown that its use yields uncertainties between 1 and 2 MeV in the saturation energy for symmetric nuclear matter.

A point of departure from the approximations described above emerges after considering Fig. 2, where we plot the difference $\delta\Sigma \equiv \Sigma - \langle \Sigma \rangle$, as a function of x and q , for

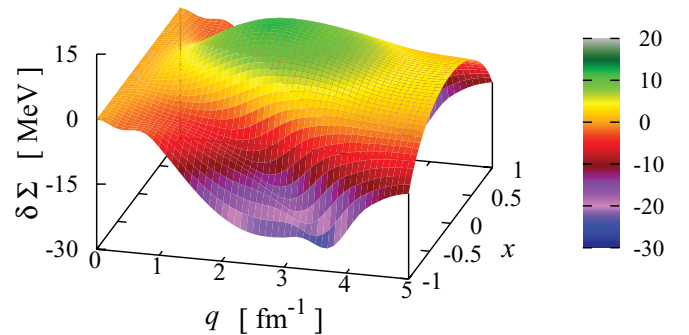


FIG. 2. (Color online) Plot of the difference $\Sigma - \langle \Sigma \rangle$ as a function of q and x , for $K = 3k_F$. Here the Pauli blocking operator allows $-1 \leq x \leq 1$. The color code for the vertical axis is given in MeV.

$K = 3k_F$ ($k_F = 1.36 \text{ fm}^{-1}$). Here also $\langle \rangle$ denotes the angular average,

$$\langle \Sigma \rangle = \frac{1}{\Delta} \int_0^\Delta \Sigma(K, q, x) dx, \quad (5)$$

with Σ calculated from the self-consistent U obtained within the RAv approach, using the continuous choice, for the Argonne v_{18} (AV18) potential [18]. Differences between Σ and its average $\langle \Sigma \rangle$ become evident, resembling a humpback symmetrically curved in x . Physically, the sign of the curvature affects the orientation of \mathbf{q} relative to \mathbf{K} , with negative curvature privileging $x = \pm 1$, a configuration mostly influenced by the Pauli exclusion (cf. Fig. 1). Conversely, positive curvature favors $x = 0$, i.e., particles with matching momenta ($p = k$). In the absence of curvature no preferred orientation to the intermediate-state kinematics is dictated by the mean field Σ , leaving \hat{q} and \hat{K} uncorrelated.

A. The angular correlation form factor

To retain the angular dependence of Σ in the energy denominator of the propagator $Q/e^{(+)}$, for a given k_F we have resorted to the following representation:

$$\Sigma \rightarrow \Sigma_x \equiv \alpha + \gamma x^2, \quad (6)$$

with α and γ functions of K and q . A linear term of the form βx would be needed in the case of asymmetric nuclear matter. To obtain α and γ we minimize $\int_{-\Delta}^{\Delta} (\Sigma - \Sigma_x)^2 dx$, leading to simple algebraic solutions. In Fig. 3(a) we show the resulting mean field α , while in Fig. 3(b) we plot the corresponding ‘‘humpback curvature’’ $\gamma \Delta^2$ as functions of q , for selected values of $2K/k_F$. These curves are based on self-consistent fields $U(k)$ at $k_F = 1.5 \text{ fm}^{-1}$ for the AV18 potential. While α as a function of q follows the same trend of U , the humpback curvature is more structured, crossing the axis at low momenta and remaining negative for large q .

The interesting feature of the angular structure of Σ_x is that it enables the exact (analytic) evaluation of the solid-angle

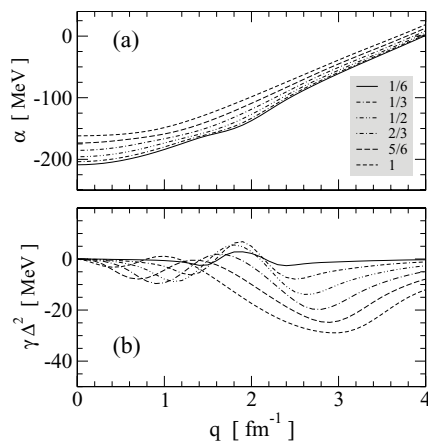


FIG. 3. (a) The mean field α and (b) corresponding humpback curvature $\gamma \Delta^2$ as functions of q for different $2K/k_F$ ratios, as listed in the legend. These results are based on the AV18 potential for $k_F = 1.5 \text{ fm}^{-1}$.

integral of the pp propagator in Eq. (3). To keep focus on the emerging structures, we have chosen at this stage to neglect couplings among different angular momentum states and take the monopole average of the ratio $Q/e^{(+)}$. The extension beyond this approximation is, in principle, straightforward. Thus, we evaluate analytically the monopole integral involving spherical harmonics, namely,

$$\lambda(K, q) = \left\langle \frac{Q}{e + i\eta} \right\rangle \equiv \int d\Omega_q Y_0^0(\hat{q}) \frac{Q}{e + i\eta} Y_0^0(\hat{q}), \quad (7)$$

leading to

$$\lambda(K, q) = \int_0^\Delta \frac{dx}{E + i\eta - \gamma x^2}, \quad (8)$$

where $E = E(K, q)$, with

$$E = \omega - \frac{K^2}{4m} - \frac{q^2}{m} - \alpha(K, q). \quad (9)$$

We can now evaluate exactly the integral on x in Eq. (8). The simplest case appears when $\gamma \equiv 0$, so that $\lambda = \Delta/(E + i\eta)$, recovering the propagator based on the traditional RAv approach. However, if γ is a nonzero function we write

$$\lambda = \mathcal{P} \int_0^\Delta \frac{dx}{E - \gamma x^2} - i\pi \int_0^\Delta \delta(E - \gamma x^2) dx, \quad (10)$$

where \mathcal{P} denotes principal value. Here special care must be paid to the roots of $E - \gamma x^2$, occurring in terms of x and/or q . The former case requires $s \equiv \gamma \Delta^2/E > 0$, allowing the root $x = \sqrt{E/\gamma}$, provided $s > 1$. The latter occurs when $\gamma(K, q)$ vanishes at q_0 , the same zero of E . In this case we use Taylor series expansions for the energy, namely, $E \sim E'_0(q - q_0)$, and the humpback function, $\gamma \sim \gamma'_0(q - q_0)$, with the primed symbol denoting partial derivative with respect to q and the subscript ‘‘o’’ indicating evaluation at q_0 . In this *double-zero* scenario the δ term contributes with $-i\pi \delta(q - q_0) \int_0^\Delta dx/|E'_0 - \gamma'_0 x^2|$, which in the absence of a zero in the denominator leads to an expression analogous to the one obtained for the principal-value integral. However, when $s_1 \equiv \gamma'_0 \Delta^2/E'_0 > 1$, the integral becomes undefined, a situation which would require higher order terms in the expansion of Σ . Actual computational runs show no occurrence of this condition, so that excluding this case we express

$$\lambda(K, q) = \frac{\Delta}{E} F(s) - i\pi \frac{\Delta}{|E|} \frac{\Theta(s-1)}{2\sqrt{s}} - i\pi \frac{\Delta}{|E'_0|} F(s_1) \delta(q - q_0), \quad (11)$$

where

$$F(s) = \frac{\tan^{-1} \sqrt{-s}}{\sqrt{-s}} \Theta(-s) + \frac{1}{2\sqrt{s}} \ln \left| \frac{1 + \sqrt{s}}{1 - \sqrt{s}} \right| \Theta(s), \quad (12)$$

with $s \neq 1$.

The above closed form for $\lambda(K, q)$ captures information regarding the angular structure exhibited by Σ . We note that the real part of the propagator factors out the whole structure implied by the humpback curvature by means of the form factor F . As illustrated in Fig. 4, $F(s)$ is a positive definite function with a logarithmic singularity at $s = 1$, continuous at $s = 0$,

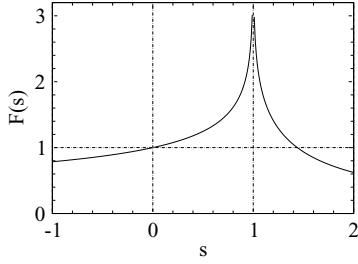


FIG. 4. The angular correlation form factor, a positive-definite function with a logarithmic singularity at $s = 1$.

where $F(0) = 1$. These features and their natural dependence on $\gamma \Delta^2$ led us to name F *angular correlation form factor*. The framework where $\lambda(K, q)$ is used as in Eq. (11) shall be called the angle-correlated (AC) approach.

In the context of the integral equation for the g matrix [cf. Eq. (1) in the AC approach], the intricate dependence of λ on q through the ratio $\gamma \Delta^2/E$, prevents a straightforward identification of sectors in q where special caution may be required. This is particularly so noting that $F[s(q)]$ diverges when $\gamma \Delta^2 \sim E$, while it vanishes when $E = \omega - \alpha - K^2/4m - q^2/m \rightarrow 0^\pm$, under which $s(q) \rightarrow \pm\infty$. Also, the unusual form of the imaginary part in terms of a step and delta functions calls for a close scrutiny to its role in the BBG equation. None of these structures would have been identified nor characterized using numerical quadrature alone in the evaluation of the monopole integral in Eq. (7). These unique aspects led us to test diverse strategies to explore features and subtleties of the solutions. The evaluation of g followed the discretization in momentum space of the BBG equation $g = v + v\lambda g$, with subsequent use of matrix inversion techniques [15].

It is worth stressing that the features disclosed here for the pp propagator are intrinsic in the sense that they emerge from the genuine behavior of the energy denominator in the angular variable x . This statement is supported by the following observation. Consider the real part of energy denominator for the exact sp fields,

$$e(q, x) \equiv \omega - \frac{K^2}{4m} - \frac{q^2}{m} - \Sigma(K, q, x). \quad (13)$$

An accurate evaluation of the monopole integral, $\frac{1}{\Delta} \int_0^\Delta dx/[e(q, x) + i\eta]$, requires analytical control of the behavior of $e(q, x)$ near x_\circ , its zero in x . To this purpose, and taking into account that $e(q, x)$ is symmetric in x , let us introduce an auxiliary energy denominator with the following quadratic form in x :

$$d(q, x) \equiv \frac{1}{2x_\circ} \left. \frac{\partial \Sigma}{\partial x} \right|_{x=x_\circ} (x_\circ^2 - x^2). \quad (14)$$

In the limit $x \rightarrow x_\circ$, these energies satisfy $e(q, x) \rightarrow d(q, x)$, matching their zero and gradient at the zero. Here we have assumed single roots in x^2 , and that the gradient term can be smoothly extrapolated to regions in q with no zeros in x . Clearly the gradient in Σ plays the role of the humpback function, $\gamma \sim (x_\circ/2)(\partial \Sigma/\partial x)|_{x_\circ}$.

Considering the above definition for d , we now express the exact propagator as

$$\frac{1}{e + i\eta} = \left(\frac{1}{e + i\eta} - \frac{1}{d + i\eta} \right) + \frac{1}{d + i\eta}.$$

As shown in Appendix A, the term in parentheses on the right-hand side is real and smooth in x and q . Thus, its contribution affects only the principal-value part of the propagator. The second term, in turn, conveys all the AC features we have already discussed, with contributions in both real and imaginary parts of the propagator according to Eq. (11) for λ . In this regard, we can safely state that the features we have disclosed for the pp propagator, particularly its imaginary part, are genuine. The extent to which they are accounted for by means of the χ^2 optimization [cf. Eq. (6)] is a matter of further investigation. In this sense the present work sets a benchmark for further studies on the subject.

B. Computational considerations

During self-consistent iterations we found that $F[s(q)]$ differs from unity mainly near q_\circ , as illustrated in Fig. 5(a) (red curve) for a typical example. Here F exhibits an extremely sharp peak due to the logarithmic singularity, and a pit due to the zero of E . Their extreme proximity illustrates how swift $s(q)$ may vary with respect to q . During self-consistent calculations both the total momentum $\mathbf{K} = \mathbf{k} + \mathbf{p}$ and starting energy $\omega = \epsilon_k + \epsilon_p$ become changing quantities, leading to changes in the position and shape of the peak. These features may become a source of instabilities, an aspect which we were able to control with the use of a generalized Weierstrass-Gauss transform of width σ , namely,

$$\bar{F}(q) = \mathcal{N} \int_{-\infty}^{\infty} F[s(p)] e^{-(q-p)^2/\sigma^2} dp, \quad (15)$$

with \mathcal{N} a normalizing constant. This transformation blurs the sharp structures in momentum space, confining the spatial

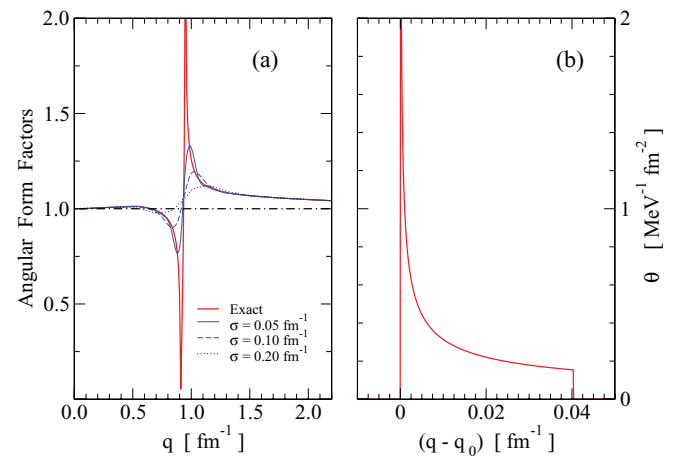


FIG. 5. (Color online) (a) Exact form factor F (red curve) and blurred angle-correlated form factors \bar{F} as functions of q for $k_F = 1.35 \text{ fm}^{-1}$, $\omega = 80 \text{ MeV}$, and $K = 3.8 \text{ fm}^{-1}$. RAv approaches yield $F(s) = 1$ (dot-dashed line). (b) Typical behavior of the step-related distribution $\theta(q)$, Eq. (16), as a function of $(q - q_\circ)$.

range of their effects. Clearly $\sigma \rightarrow 0$ restores the original function, $\bar{F}(q) \rightarrow F[s(q)]$. In Fig. 5(a) we plot $\bar{F}(q)$ as a function of q for $\sigma = 0.05, 0.10$, and 0.20 fm^{-1} . The findings reported in this work are based on $\sigma = 0.05 \text{ fm}^{-1}$ (solid blue curve), which provides sound stability to the results to be discussed later on.

Regarding the imaginary contributions, we have found that the condition $s(q) > 1$ is met over an extremely narrow band in q , with the pole q_0 at one of its boundaries. The width of the band is typically a fraction of fm^{-1} . In Fig. 5(b) we show the step-related distribution

$$\theta(q) = q^2 \frac{\Delta}{|E|} \frac{\Theta(s-1)}{\sqrt{s}}, \quad (16)$$

as a function of $(q - q_0)$ under the same conditions used for Fig. 5(a). Observe the narrowness of the width, of the order of $\sim 0.4 \text{ fm}^{-1}$ in this case, featuring a singular behavior $\sim 1/\sqrt{|q - q_0|}$ at the pole. These narrow structures make the use of traditional quadratures unsuitable if no caution is made to reproduce the strength of the distribution

$$S = \int_0^\infty \theta(q) dq. \quad (17)$$

Otherwise the contribution of $\theta(q)$ to the imaginary part of λ would become erratic, subject to whether or not the band in q is reached by the mesh $\{q_i\}$ used for the quadrature in q . To control these features, if q_0 exists but all $\theta(q_i) \equiv \theta_i$ are zero, then we give to $\text{Im } \lambda(K, q)$ the Dirac δ -function (double-zero) form. Otherwise we modify

$$\theta_i \rightarrow \frac{S}{\sum_{\theta_j \neq 0} \theta_j w_j} \theta_i,$$

with $\{w_i\}$ the set of weights used for the quadrature in q . An accurate evaluation of S is described in Appendix B. This construction guarantees numerically that $S = \sum_i w_i \theta_i$, a consideration which proved crucial to prevent spurious fluctuations of the mass operator, particularly near the Fermi surface. Still, as shown in that appendix, the strength exhibits a discontinuity depending on whether the condition $s > 1$ occurs below or above q_0 , leading to changes in the absorptive part of the g matrix.

Since most of the nontrivial structure of $\lambda(K, q)$ occurs in the vicinity of q_0 , we use an N -point Gaussian quadrature in the interval $[0, q_0]$, supplemented with M Gaussian points mapped [19] as $q_i = q_0 + \bar{q} \tan[\pi(u_i + 1)/4]$. Here \bar{q} is adjusted so that $q_M \sim 500 \text{ fm}^{-1}$ ($M = 25$), while N is set to yield a balanced density of points on each side of the pole ($N \approx M\sqrt{2q_0/\pi\bar{q}}$). The adequacy of this quadrature was tested in free space ($k_F = 0$), comparing the resulting np phase shifts with those reported by the Argonne [18] and Paris [20] groups. The agreement with the reported values is quite satisfactory, reproducing to full digits most of the published phase shifts. Self-consistency is imposed requiring that the maximum variations of $U(k)$ on three consecutive iterations do not exceed 0.05 MeV , in the range $0 \leq k \leq 5.5 \text{ fm}^{-1}$. The Fermi integral $|\mathbf{p}| \leq k_F$ in Eq. (2) is performed by means of Gaussian quadrature for \mathbf{p} . The findings reported in this work consider solutions of Eq. (3) to all NN states with total angular momentum up to $J = 7$ and 9. Additional

waves (out to $J = 15$) were also included within the Born approximation for the g matrix [21], using the long-range one-pion-exchange potential of Ref. [22].

III. RESULTS AND DISCUSSION

A. Symmetric nuclear matter

Results for the on-shell mass operator are shown in Fig. 6 as functions of k for $k_F = 1.20$ (0.05) 1.75 fm^{-1} . Figures 6(a) and 6(b), and 6(c) and 6(d) correspond to results based on the RAv and AC approaches, respectively. The upper (lower) frames display results for their corresponding real (imaginary) components. The outermost blue (red) curves denote $k_F = 1.20$ (1.75 fm^{-1}). These results are based on the AV18 bare potential.

Although the real component of the self-consistent fields obtained from the two approaches are very similar below k_F , for $k > k_F$ clear differences do appear, being more pronounced as k_F increases. In the case of $\text{Re } M(k, \epsilon_k)$, the RAv approach is characterized by uniform growth with common interceptions at k near 3.5 fm^{-1} . In contrast, the AC results show inflection points in the interval between 2.5 and 4 fm^{-1} . The differences between the two approaches are less pronounced for the blue curves, i.e., $k_F < 1.3 \text{ fm}^{-1}$. In the case of $\text{Im } M(k, \epsilon_k)$, the RAv approach leads to a monotonic descent while the AC results also show inflection points, more pronounced at the higher k_F . We have investigated the origin of such differences and found that they are correlated with the side relative to q_0 where the condition $s > 1$ occurs more frequently. As discussed in Appendix B, the strength S in Eq. (17) experiences a discontinuity when the condition $s = 1$ is met, which may occur to the right or to the left of the pole

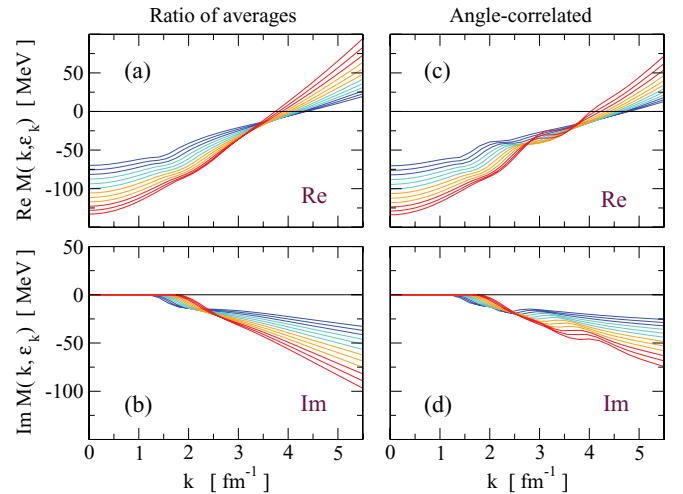


FIG. 6. (Color online) On-shell mass operator at various Fermi momenta. RAv results are shown in (a) and (b), while AC results are shown in (c) and (d). The upper and lower frames correspond to the real and imaginary parts of the mass operator, respectively. The outermost blue (red) curves correspond to $k_F = 1.20$ (1.75 fm^{-1}). The k_F difference between consecutive curves is 0.05 fm^{-1} . These results are based on the AV18 bare potential.

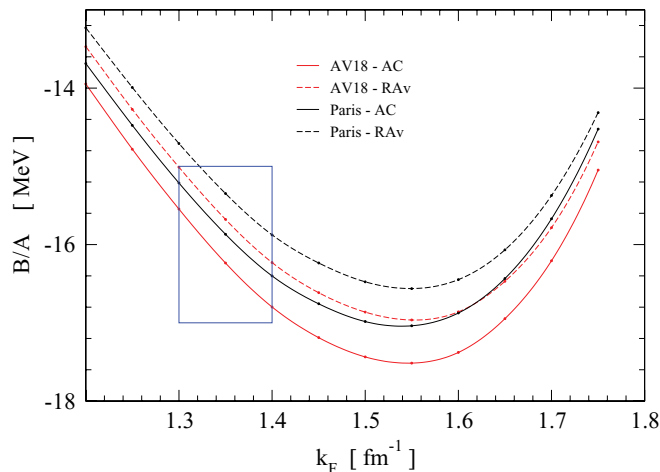


FIG. 7. (Color online) Saturation curves (B/A vs k_F) for the AV18 (red curves) and Paris (black curves) NN potentials based on the AC (solid curves) and RAv (dashed curves) approaches, respectively. The box denotes the accepted sector for the saturation point.

q_0 . This feature affects directly the trend of the imaginary part of g and its subsequent contribution to the mass operator.

Saturation properties of NM constitute a natural ground to assess the effects of angular correlations as they emerge from the actual $\lambda(K, q)$. In Fig. 7 we show saturation curves (B/A vs k_F) for the AV18 (red curves) and Paris (black curves) NN potentials based on the RAv approximation (dashed curves) and AC approach (solid curves). The small circles denote the actual calculated values, while the curves are the result of cubic spline interpolations. The box denotes the accepted sector for the saturation point, namely, $k_F = 1.35 \pm 0.05 \text{ fm}^{-1}$ and $B/A = -16 \pm 1 \text{ MeV}$. The results shown in this figure take into account $J_{\max} = 15$, with the first nine waves actual solutions of Eq. (3) and the remaining six obtained within the Born approximation. It becomes clear from this figure that the inclusion of angular correlations yields an increase in the binding at the saturation point by about 0.5 MeV, with AV18 binding slightly more than the Paris potential. We have explored other NN realistic potentials and find similar trends.

A more detailed account of some of our findings are summarized in Table I, where we show results for the saturation Fermi momentum k_F , binding energy per nucleon B/A , and incompressibility K_{nm} following the AC and RAv approaches, for the AV18 and Paris potentials. Here

$$K_{nm} = k_F^2 \frac{\partial^2(B/A)}{\partial k_F^2}, \quad (18)$$

with the second derivative evaluated at the saturation momentum k_F . To assess convergence on the number of partial waves, we have examined the cases $J_{\max} = 7, 9$, and 15. Here we denote by 15^a and 15^b the cases where the Born approximation is applied in the last eight and six partial waves, respectively.

We have found that the evaluation of the incompressibility is sensitive to the choice of interpolation method of B/A in terms of k_F . The results reported here were obtained using two distinct schemes: cubic spline and Padé P[2,2] interpolations. While both methods agree on the saturation points out to three

TABLE I. Nuclear matter saturation properties based on the angle-correlated and ratio-of-averages representations of the pp propagator for the AV18 and Paris potentials. See the text for explanation of the numbers quoted in parentheses.

λ	J_{\max}	AV18			Paris		
		k_F (fm^{-1})	B/A (MeV)	K_{nm} (MeV)	k_F (fm^{-1})	B/A (MeV)	K_{nm} (MeV)
$\langle \frac{\rho}{e^{(+)}} \rangle$	7	1.53	-16.7	190(2)	1.53	-16.1	178(1)
	9	1.53	-16.9	192(2)	1.54	-16.4	188(3)
	15^a	1.54	-17.1	199(4)	1.54	-16.5	191(3)
	15^b	1.54	-17.0	196(3)	1.55	-16.6	193(4)
$\langle \frac{\rho}{e^{(+)}} \rangle$	7	1.53	-17.2	194(2)	1.53	-16.5	182(1)
	9	1.54	-17.4	198(3)	1.55	-16.8	198(4)
	15^a	1.55	-17.6	207(7)	1.55	-16.9	201(5)
	15^b	1.55	-17.5	203(6)	1.55	-17.0	204(6)

^{a,b}See text for explanation.

significant figures, the calculated incompressibility may differ up to 14 MeV. In the K_{nm} column of Table I we report the average obtained from the two methods, quoting in parentheses their difference relative to the average.

When comparing the RAv and AC approaches, we observe that angular correlations yield an increase of 0.4–0.5 MeV in the saturation energy relative to the angle-averaged results, a trend observed regardless of the number of partial waves included. While the Paris potential predictions for the saturation energy remain within accepted range, the inclusion of angular correlations sets the AV18 below the lower bound for accepted value. From Table I we also note that, in all cases, the saturation energy increases by about 0.3–0.5 MeV in going from 7 to 15 partial waves. On the other hand, all cases overestimate the saturation density by 45–50 % relative to the accepted empirical value ($k_F = 1.53\text{--}1.55 \text{ fm}^{-1}$). Regarding the incompressibility, a moderate increase of 4 to 11 MeV is observed when angular correlations are taken into account. A similar trend occurs in going from 7 to 15 partial waves, with the AV18 potential calculations affected by 6–13 MeV while those for the Paris potential are affected by 15–22 MeV.

We have also examined the differences between the AC and RAv self-consistent fields at low densities. These differences diminish with decreasing k_F , as expected, making unnecessary the treatment of angular correlations at low k_F .

B. Nucleon-nucleus elastic scattering

A substantial body of research has been devoted toward the development of microscopic descriptions for nucleon-nucleus collisions based on NN effective interactions [8,23]. These interactions are calculated directly from realistic models for the bare NN interaction by solving the BBG equation. In the microscopic approach of Arellano, Brieva, and Love [24,25], the genuine off-shell g matrix is folded in momentum space with the target ground-state mixed density, leading to energy-dependent nonlocal optical potentials. No localization procedure is applied to the calculated g matrix.

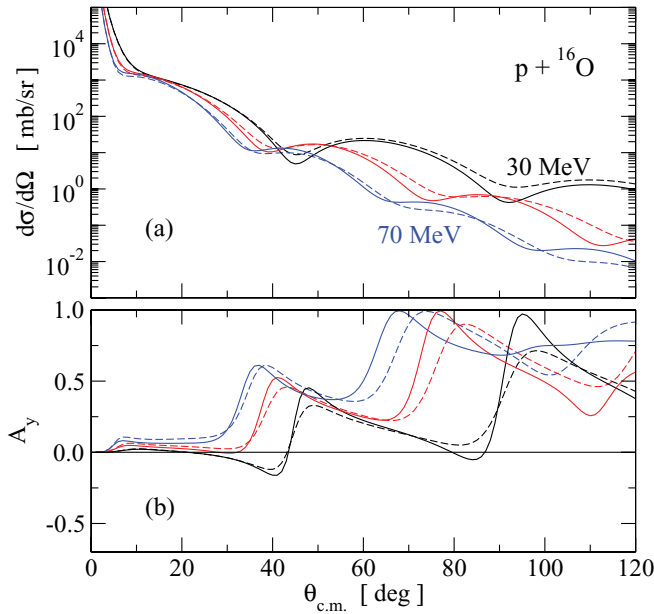


FIG. 8. (Color online) (a) Differential cross sections $d\sigma/d\Omega$ and (b) analyzing power $A_y(\theta)$, as functions of the center-of-mass scattering angle $\theta_{c.m.}$ for $p+{}^{16}\text{O}$ elastic scattering, as obtained from momentum space g -matrix folding optical model potentials. The solid and dashed curves represent results based on the AC and RAV approaches, respectively. Blue, red, and black curves correspond to beam energies of 30, 50, and 70 MeV, respectively.

In order to assess the impact of angular correlations on nucleon scattering from nuclei, we have calculated the scattering observables for proton elastic scattering from ${}^{16}\text{O}$ at energies between 30 and 70 MeV. The optical potentials are based on g matrices within the AC and RAV approaches, each set calculated with their corresponding self-consistent solutions. Here we have chosen the AV18 potential as the bare NN interaction.

In Fig. 8 we show the differential cross sections ($d\sigma/d\Omega$) and analyzing power (A_y) as functions of the scattering angle in the center-of-mass reference frame ($\theta_{c.m.}$), for proton elastic scattering from ${}^{16}\text{O}$. The blue curves denote the results at 30 MeV, red curves at 50 MeV, and black curves at 70 MeV. The solid and dashed curves represent results based on the AC and RAV approaches, respectively.

From these results the sensitivity of elastic scattering to the treatment of the angular correlations in the pp propagator becomes clear. The effect in all cases is a more diffractive pattern in the cross section, together with more pronounced peaks in A_y . These results are not necessarily in disagreement with the findings reported by Cheon and Redish in Ref. [14]. While here we focus on beam energies below 100 MeV, in the referred work the study was performed for energies above 200 MeV, treating the energy denominator within an effective-mass approximation but including the multistate coupling due to the nonsphericity of the Pauli blocking. As mentioned before, the effective-mass approximation implies $F(s) = 1$, therefore it neglects the angular correlations treated in this work. On the other hand, we have not treated the multistate coupling at this stage due to the nonsphericity of the whole

propagator Q/e . In any case, from this exploratory application it becomes clear that significant effects may lay behind an exact treatment of the angular dependence of the pp propagator. The extent to which they remain, change, or average away is a matter of further research.

IV. SUMMARY AND CONCLUSIONS

We have investigated the effects stemming from the angular dependence of the energy denominator of the pp propagator in symmetric nuclear matter, where its explicit angular behavior is retained by means of a quadratic expansion in terms of $x = \hat{K} \cdot \hat{q}$. Following an exact angular integration in the monopole approximation we provide analytic expressions for the propagator, characterized by an angular-correlation form factor and an additional imaginary term in the form of a step function. These features in the pp propagator lead to sharp structures in momentum space, which in the context of the BBG equation were controlled by means of a Gauss-Weierstrass transformation of narrow width. Self-consistent solutions for the mass operator based on this angle-correlated approach were compared with those obtained within the traditional approaches, where angular averages are used separately for the Pauli blocking and the energy denominator (RAV). Studies based on the AV18 and Paris NN potentials show that the saturation energy deepens slightly, by about 0.5 MeV, relative to the RAV approach, whereas the saturation density remains overestimated by $\sim 50\%$ relative to its empirical value. We also note that angular correlations change only marginally the incompressibility. Differences for the self-consistent solutions from these two approaches diminish with decreasing k_F , as expected.

We also investigated the effects of angular correlations on proton-nucleus elastic scattering at beam energies between 30 and 70 MeV. Here the fully off-shell g matrix, obtained within AC and RAV approaches, are used to calculate microscopic optical model potentials. We find clear sensitivity of the scattering observables to considerations in the treatment of the pp angular correlations. The RAV approach smoothens the diffractive minima of $d\sigma/d\Omega$, while the extreme values of A_y are slightly diminished. Preliminary investigations suggest that these effects diminish with the energy of the beam, something which is understandable because medium effect become less important as the energy of the beam increases. In that sense, our findings are consistent with the ones reported in Ref. [14] for intermediate-energy nucleon scattering. In any case, the trend we observe at energies below 100 MeV indicates the need for a closer investigation of the role of pp angular correlations on nucleon-nucleus scattering.

Correlations arising from averaging the ratio Q/e have a counterpart in the statistical theory of nuclear reactions. In the Hauser-Feshbach theory of compound nucleus (CN) reactions, the assumption made is that the exit channels have lost memory of how the CN was formed in the incoming channels. Actually, it has been demonstrated [26,27] that the incoming and exit channels display correlations. Again, these studies illustrate the point that in the presence of correlations, the average of a ratio may differ from the ratio of the averages.

The study presented here for the treatment of the pp propagator is incomplete in two aspects. First, in that the angular structure of the energy denominator is given a parabolic dependence, a feature which can be improved if the exact sp fields are used. A way to treat these fields exactly has been sketched in Sec. II A. Second, we have not treated the full entanglement between different states, as it would emerge when the full x dependence in Eq. (3) is treated exactly. It has been reported [13] that the incorporation of the coupling between different states due to the nonsphericity of the Pauli blocking yield important corrections, moving the calculated saturation point closer to the empirical value. These findings need to be investigated further when angular correlations are taken into account.

The findings disclosed here, particularly the features exhibited by the angular-correlation form factor, may be a source of additional corrections in high-precision studies of symmetric as well as asymmetric nuclear matter. Moreover, recent developments involving sophisticated relativistic and nonrelativistic calculations [28], including three-body forces [6,29,30], finite temperature [31], higher order terms in the hole-line expansion [4,32], or the development of low-momentum NN interactions [33], rely upon the RAV approach in the form of effective-mass approximations or angle-averaged energy denominators. Although it is premature to anticipate the actual implications of AC effects on these state-of-the-art applications, their inclusion would either alter their current predictions and/or set narrower margins of uncertainty in their account of conventional effects.

ACKNOWLEDGMENTS

The authors are indebted to Arnau Rios (University of Surrey, UK) for valuable comments. H.F.A. acknowledges funding and the generous hospitality of colleagues at CEA/DAM/DIF, Bruyères-le-Châtel, France, during his sabbatical leave where part of this research was carried out. This work was funded in part by FONDECYT under Grant No. 1080471.

APPENDIX A: REGULARIZATION OF THE EXACT PROPAGATOR

Here we show that $[1/e^{(+)} - 1/d^{(+)}]$ is real, vanishing when $x \rightarrow x_0$, the zero of $e(q, x)$. In this way we demonstrate that the behavior of the imaginary part of the exact propagator is fully accounted for by $1/d^{(+)}$, validating the expressions for the imaginary part of the propagator in Eq. (11). The analysis here is focused on regions of q where there are zeros in the exact denominator, keeping in mind that near the zero $d(q, x) \approx [\frac{1}{2x_0}(\partial e/\partial x)_{x_0}](x^2 - x_0^2)$.

Considering the identity

$$\frac{1}{u + i\eta} = \frac{u}{u^2 + \eta^2} - \frac{i\eta}{u^2 + \eta^2},$$

we obtain for the real and imaginary parts

$$X(q, x) \equiv \text{Re} \left\{ \frac{1}{e + i\eta} - \frac{1}{d + i\eta} \right\} = \frac{(e - d)(\eta^2 - ed)}{(e^2 + \eta^2)(d^2 + \eta^2)}$$

and

$$Y(q, x) \equiv \text{Im} \left\{ \frac{1}{e + i\eta} - \frac{1}{d + i\eta} \right\} = \frac{\eta(e^2 - d^2)}{(e^2 + \eta^2)(d^2 + \eta^2)},$$

respectively. For a given q but away from x_0 , then $e \neq 0$ and $d \neq 0$. If we subsequently let $\eta \rightarrow 0$, then X becomes finite ($X \rightarrow 1/e - 1/d$) while Y vanishes. The other case is when $x = x_0$, so that $e = d = 0$, leading to $X = Y = 0$. The subsequent limit $\eta \rightarrow 0$ does not alter the result. Therefore $X(q, x)$ is indeed a real and finite function, while $Y(q, x) \equiv 0$.

APPENDIX B: EVALUATION OF THE STRENGTH S

Here we describe the method used to evaluate the strength S defined by Eq. (17). The integral is confined to the region where $s \geq 1$. One of its boundaries is given by the condition $E = \gamma \Delta^2$. Since both E , as expressed by Eq. (9), and γ are smooth functions, the solution to this equation is straightforward, leading to a single root b near q_0 located on either side of q_0 . The other boundary occurs at q_0 , with q approaching q_0 from that side where $s \rightarrow +\infty$. If we denote $\gamma_0 = \gamma(K, q_0)$, then near q_0 we can approximate $s \approx \gamma_0 \Delta^2 / E'_0(q - q_0)$. Thus, $s \rightarrow +\infty$ occurs on the right side of q_0 as long as $\gamma_0 / E'_0 > 0$. If this ratio is negative, the condition $s > 1$ is met on the left side of q_0 , leading to $b < q_0$.

Once b is determined we proceed to evaluate $S = \int_0^\infty \theta(q) dq$. The integral is confined to the interval $[q_1, q_2]$ where the condition $s > 1$ is met. Explicitly,

$$S = \int_{q_1}^{q_2} \frac{q^2 dq}{\sqrt{\gamma E}}.$$

In order to control the singular behavior of the integrand near q_0 , we subtract (and add) the term $q_0^2 / \sqrt{a(q - q_0)}$, where $a = \gamma_0 E'_0 / 2q_0$. Here we assume no double zero, so that $a \neq 0$. With this construction we express S as the sum of two integrals, $S = S_0 + \Delta S$, where

$$S_0 = \int_{q_1}^{q_2} \frac{q_0^2 dq}{\sqrt{a(q^2 - q_0^2)}}. \quad (\text{B1})$$

The evaluation of $\Delta S = S - S_0$ involves a nonsingular integrand, so that a simple Gaussian quadrature can be used. For S_0 in Eq. (B1), instead, we evaluate analytically

$$S_0 = \frac{q_0^2}{\sqrt{|a|}} \times \begin{cases} \arccos(t) & \text{if } t = b/q_0 < 1 \\ \ln(t + \sqrt{t^2 - 1}) & \text{if } t > 1. \end{cases} \quad (\text{B2})$$

We can now explore the behavior of S_0 when b is near q_0 . The boundary b is obtained imposing $s = 1$, or equivalently $E = \gamma \Delta^2$. Expanding both sides to first order around q_0 we obtain $E'_0(b - q_0) = [\gamma_0 + \gamma'_0(b - q_0)]\Delta^2$. Therefore

$$b \approx q_0 + \frac{\gamma_0 \Delta^2}{E'_0 - \gamma'_0 \Delta^2}.$$

Considering that the denominator is always negative—feature observed numerically—then the position of the boundary b with respect to q_0 is given by the sign of the humpback curvature at the pole, i.e., γ_0 . With these considerations and using the definition for a , we get

$$S_0 \sim \frac{2q_0^2}{|E'_0|\sqrt{1-s_1}} \times \begin{cases} \frac{\pi}{\sqrt{2(1-t)}} & \text{if } t < 1 \\ 1 & \text{if } t > 1, \end{cases} \quad (\text{B3})$$

where $s_1 = \gamma'_0 \Delta^2 / E'_0$. Here it becomes evident that there exists a discontinuity in S_0 when the boundary b passes from one side of q_0 to the other. This transit is driven by the sign of γ_0 . The

double-zero contribution in Eq. (11) is coincident with this result when $t > 1$ and $t \rightarrow 1$.

The above expression for S_0 also exhibits a singularity when b approaches q_0 from the left. Although there is no reason to discard these occurrences, we have monitored this quantity during self-consistent procedures and found no indication of diverging S_0 . Isolated events may occur when the Fermi motion integration in Eq. (2) is performed. In practice any event where $|b - q_0| < 10^{-2} \text{ fm}^{-1}$ is treated as a double zero, where simultaneously $\epsilon_k + \epsilon_p = K^2/4m + q_0^2/m + \Sigma(K, q_0) = 0$ and $\gamma(K, q_0) = 0$, with $\mathbf{K} = \mathbf{k} + \mathbf{p}$.

-
- [1] *Nuclear Methods and the Nuclear Equation of State*, edited by M. Baldo, International Review of Nuclear Physics Vol. 8 (World Scientific, Singapore, 1999).
- [2] W. H. Dickhoff and D. Van Neck, *Many-Body Theory Exposed!* (World Scientific, Singapore, 2005).
- [3] B. D. Day, *Phys. Rev. Lett.* **47**, 226 (1981).
- [4] H. Q. Song, M. Baldo, G. Giansiracusa, and U. Lombardo, *Phys. Rev. Lett.* **81**, 1584 (1998).
- [5] Y. Dewulf, W. H. Dickhoff, D. Van Neck, E. R. Stoddard, and M. Waroquier, *Phys. Rev. Lett.* **90**, 152501 (2003).
- [6] Z. H. Li, U. Lombardo, H.-J. Schulze, W. Zuo, L. W. Chen, and H. R. Ma, *Phys. Rev. C* **74**, 047304 (2006).
- [7] J. P. Jeukenne, A. Lejeune, and C. Mahaux, *Phys. Rep. C* **25**, 83 (1976).
- [8] K. Amos, P. J. Dortmans, H. V. von Geramb, S. Karataglidis, and J. Raynal, in *Advances in Nuclear Physics*, edited by J. W. Negele and E. W. Vogt (Springer, US, 2000), Vol. 25, p. 275.
- [9] D. J. Dean and M. Hjorth-Jensen, *Rev. Mod. Phys.* **75**, 607 (2003).
- [10] T. Frick, Kh. Gad, H. Mütter, and P. Czerski, *Phys. Rev. C* **65**, 034321 (2002).
- [11] F. Sammarruca, X. Meng, and E. J. Stephenson, *Phys. Rev. C* **62**, 014614 (2000).
- [12] K. Suzuki, R. Okamoto, M. Kohno, and S. Nagata, *Nucl. Phys. A* **665**, 92 (2000).
- [13] E. Schiller, H. Mütter, and P. Czerski, *Phys. Rev. C* **59**, 2934 (1999); **60**, 059901(E) (1999).
- [14] T. Cheon and E. F. Redish, *Phys. Rev. C* **39**, 331 (1989).
- [15] R. Sartor, *Phys. Rev. C* **54**, 809 (1996).
- [16] K. A. Brueckner and J. L. Gammel, *Phys. Rev.* **109**, 1023 (1958).
- [17] M. Baldo and A. Fiasconaro, *Phys. Lett. B* **491**, 240 (2000).
- [18] R. B. Wiringa, V. G. J. Stoks, and R. Schiavilla, *Phys. Rev. C* **51**, 38 (1995).
- [19] G. E. Brown, A. D. Jackson, and T. T. S. Kuo, *Nucl. Phys. A* **133**, 482 (1969).
- [20] M. Lacombe, B. Loiseau, J. M. Richard, R. Vinh Mau, J. Côté, P. Pirés, and R. de Tournell, *Phys. Rev. C* **21**, 861 (1980).
- [21] H.-J. Schulze, J. Cugnon, A. Lejeune, M. Baldo, and U. Lombardo, *Phys. Rev. C* **52**, 2785 (1995).
- [22] R. B. Wiringa, R. A. Smith, and T. L. Ainsworth, *Phys. Rev. C* **29**, 1207 (1984).
- [23] L. Ray, G. W. Hoffmann, and W. R. Coker, *Phys. Rep.* **212**, 223 (1992).
- [24] H. F. Arellano, F. A. Brieva, and W. G. Love, *Phys. Rev. C* **52**, 301 (1995).
- [25] F. J. Aguayo and H. F. Arellano, *Phys. Rev. C* **78**, 014608 (2008).
- [26] P. A. Moldauer, *Phys. Rev. C* **14**, 764 (1976).
- [27] S. Hilaire, Ch. Lagrange, and A. J. Koning, *Ann. Phys.* **306**, 209 (2003).
- [28] E. N. E. van Dalen, C. Fuchs, and A. Faessler, *Phys. Rev. C* **72**, 065803 (2005).
- [29] R. Sartor, *Phys. Rev. C* **73**, 034307 (2006).
- [30] W. Zuo, U. Lombardo, H.-J. Schulze, and Z. H. Li, *Phys. Rev. C* **74**, 014317 (2006).
- [31] A. Rios, A. Polls, A. Ramos, and H. Mütter, *Phys. Rev. C* **74**, 054317 (2006).
- [32] M. Baldo and L. Lo Monaco, *Eur. Phys. J. A* **17**, 457 (2003).
- [33] L.-W. Siu, J. W. Holt, T. T. S. Kuo, and G. E. Brown, *Phys. Rev. C* **79**, 054004 (2009).